AGU PUBLICATIONS

JGR

Journal of Geophysical Research: Oceans

RESEARCH ARTICLE

10.1002/2017JC013447

Direct Numerical Simulation of Oscillatory Flow Over a Wavy, Rough, and Permeable Bottom

Marco Mazzuoli[1], Paolo Blondeaux[1], Julian Simeonov[2], and Joseph Calantoni[2]

[1]Department of Civil, Chemical, Environmental Engineering, University of Genova, Genova, Italy, [2]Marine Geosciences Division, U.S. Naval Research Laboratory, Code 7434, Stennis Space Center, Hancock County, MS, USA

Key Points:
- Hydrodynamic force acting on sediment particles is strongly affected by coherent vortex structures propagating close to the bed
- Transition to turbulence is induced by the wavy bed at a value of the Reynolds number significantly smaller than in absence of waviness
- The time development of the bed shear stress is shown and split into the viscous, turbulent, and "form" contributions

Supporting Information:
- Supporting Information S1
- Movie S1

Correspondence to:
M. Mazzuoli,
marco.mazzuoli@unige.it

Citation:
Mazzuoli, M., Blondeaux, P., Simeonov, J., & Calantoni, J. (2018). Direct numerical simulation of oscillatory flow over a wavy, rough, and permeable bottom. *Journal of Geophysical Research: Oceans*, *123*. https://doi.org/10.1002/2017JC013447

Received 11 SEP 2017
Accepted 10 DEC 2017
Accepted article online 28 DEC 2017

Abstract The results of a direct numerical simulation of oscillatory flow over a wavy bottom composed of different layers of spherical particles are described. The amplitude of wavy bottom is much smaller in scale than typical bed forms such as sand ripples. The spherical particles are packed in such a way to reproduce a bottom profile observed during an experiment conducted in a laboratory flow tunnel with well-sorted coarse sand. The amplitude and period of the external forcing flow as well as the size of the particles are set equal to the experimental values and the computed velocity field is compared with the measured velocity profiles. The direct numerical simulation allows for the evaluation of quantities, which are difficult to measure in a laboratory experiment (e.g., vorticity, seepage flow velocity, and hydrodynamic force acting on sediment particles). In particular, attention is focused on the coherent vortex structures generated by the vorticity shed by both the spherical particles and the bottom waviness. Results show that the wavy bottom triggers transition to turbulence. Moreover, the forces acting on the spherical particles are computed to investigate the mechanisms through which they are possibly mobilized by the oscillatory flow. It was found that forces capable of mobilizing surface particles are strongly correlated with the particle position above the mean bed elevation and the passage of coherent vortices above them.

1. Introduction

Vortex structures generated through the interactions of the flow with a natural sandy bottom may play a key role in sediment transport processes. It is known that locally vortex structures generate high values of shear stress on the bed; however, these structures may be small and difficult to measure in the field or laboratory. High values of local bed shear stress may dislodge particles. Once a particle is dislodged, it either rolls and slides along the bottom profile or is picked up and transported in suspension, depending on the ratio of the fall velocity of the sediment particle to the local vertical velocity induced by the vortex structures.

The evaluation of the limiting conditions, above which the sediment particles start to move or are carried into suspension, is a complex problem. Indeed, to quantify the bottom erodibility, it is necessary to know both the mechanical properties of the bottom material (e.g., grain size, grain density, grain shape, history of deposition and erosion, and biological factors (Le Hir et al., 2007)) and the dynamics of the vortices present close to the bottom that may induce, locally, large values of the forces acting on the sediment particles. The vortices may be generated either by flow separation around the sediments or by an intrinsic instability of large-scale, coherent vortex-structures, which might induce a local increase of the bottom shear stress.

To understand the basic mechanisms controlling sediment transport, the interaction of loose particles with vortex structures has been extensively investigated (see review papers by Soldati & Marchioli, 2009, 2012). However, there are still aspects of the phenomenon which are not well known yet, in particular when the forcing flow is oscillatory. Indeed, the largest number of studies of flow and particle interaction are devoted to the investigation of steady flows, since similar investigations in unsteady flows pose formidable problems both using experimental techniques and numerical means. Moreover, almost all the previous investigations consider particles resting or moving over a smooth and flat bottom; however, in natural environments, sediment grains make the bottom rough and generate small vortices. Finally, macroroughness elements (e.g., small-scale bed forms, pebbles, and protuberances produced by benthos) may generate large-scale,

coherent vortex structures, which further enhance mixing phenomena (see the recent numerical simulations of Mazzuoli et al., 2017).

An experimental investigation considering an oscillatory flow over macroroughness elements measured the velocity within the boundary layer generated over spheres of large diameter, arranged in a hexagonal pattern (Keiller & Sleath, 1976). The measurements show the existence of coherent vortex structures, which are released by the roughness elements at flow reversal and move away from the bottom. The oscillatory flow over a similar rough bottom (the roughness being generated by semispheres glued on a plane in a hexagonal pattern) was modeled using direct numerical simulations of momentum and continuity equations (Fornarelli & Vittori, 2009). Both the experimental measurements and the numerical results show that the time development of the velocity field close to the bottom is characterized by two maxima. The first maximum is in phase with the maximum of the free stream velocity while the second relative maximum is generated when the external flow reverses its direction and it is due to the passage of the vortices, previously shed by the roughness elements, which move away from the bottom. Similar numerical simulations (Mazzuoli & Vittori, 2016) were made by substituting the semispheres with spherical particles thus obtaining a geometry more similar to that used in previous experiments (Keiller & Sleath, 1976). Two different numerical studies (Ghodke & Apte, 2016; Mazzuoli & Vittori, 2016) both considering a similar geometry, independently confirm the presence of vortices released by the roughness elements at flow reversal, a phenomenon which is also observed in laboratory experiments of oscillatory flow over regular roughness elements (Krstic & Fernando, 2001).

The number of papers describing the oscillatory flow over small-scale bed forms (ripples) is large. Moreover, the dynamics of the vortices shed by sand ripples largely depends on the bottom profile and it becomes quite complex even when periodic bottom forms are considered (Blondeaux & Vittori, 1991; Vittori & Blondeaux, 1993). Vortex dynamics over bed forms are summarized in review papers (Blondeaux, 2001; Mei & Liu, 1993) and books (Sleath, 1984; Nielsen, 1992). The vortex structures generated by bedforms such as sand ripples tend to be large and scale with the size of the bedforms, whereas the vortices considered here tend to scale more closely with particle size.

The present paper is focused on the direct numerical simulation of oscillatory flow over a wavy bottom made of several layers of spherical particles. The amplitude of the wavy bottom in our experiment and simulation is much smaller than that of typical bed forms. The spherical particles are packed in such a way to reproduce the bottom profile observed during an experiment carried out in a laboratory flow tunnel. The computed velocity field is compared with velocity measurements obtained using a profiling acoustic Doppler velocimeter. However, the main aim of the present work is the investigation of the the dynamics of the vortex structures which move close to the bottom and are difficult to measure or to visualize using any experimental apparatus. The forcing flow is assumed to be oscillatory and the amplitude and the frequency of the fluid oscillations were chosen to reproduce the measured free stream velocity in the laboratory. Consequently, the use of direct numerical simulations allowed for the evaluation of quantities that are very difficult to measure in a laboratory experiment (e.g., vorticity, dissipation, and production of turbulence). In addition to providing a detailed analysis of the flow field above the bed, the flow and pressure fields within the porous, packed sediments were also analyzed to provide information on how the vortex structures above the bed affect the fluid mechanics within the bed.

2. Numerical Methods

It is well known that, at the leading order of approximation, the flow close to the bottom of a flow tunnel (or U-tube) and the flow at the bottom of a sea wave are coincident and can be studied by considering the flow generated close to a rigid surface by an oscillating pressure gradient described by

$$\frac{\partial p^*}{\partial x_1^*} = -\rho^* U_0^* \omega^* \sin(\omega^* t^*), \quad \frac{\partial p^*}{\partial x_2^*} = 0, \quad \frac{\partial p^*}{\partial x_3^*} = 0, \tag{1}$$

where (x_1^*, x_2^*, and x_3^*) is a Cartesian coordinate system with the x_1^* axis pointing in the streanwise direction and the x_3^* axis pointing in the vertical direction (away from the bed). A star is used to denote dimensional quantities while the same symbols without the star denote their dimensionless counterparts. In (1), ρ^* is the density of the sea water, assumed to be constant, and U_0^* and $\omega^* = \frac{2\pi}{T^*}$ are the amplitude and the angular

frequency of fluid velocity oscillations induced by the the pressure gradient (T^* is the period of the oscillations). The hydrodynamic problem is written in dimensionless form introducing the following variables:

$$\begin{aligned}(x_1,x_2,x_3)&=\frac{(x_1^*,x_2^*,x_3^*)}{\delta^*} \quad ; \quad t=t^*\omega^* \; ; \\ (u_1,u_2,u_3)&=\frac{(u_1^*,u_2^*,u_3^*)}{U_0^*} \quad ; \quad p=\frac{p^*}{\rho^*(U_0^*)^2} \quad ; \quad (f_1,f_2,f_3)=\frac{(f_1^*,f_2^*,f_3^*)}{U_0^*\omega^*} \; .\end{aligned} \tag{2}$$

In (2), t^* is time, u_1^*, u_2^*, and u_3^* are the fluid velocity components along the x_1^*, x_2^*, and x_3^* directions, respectively, (f_1^*, f_2^*, f_3^*) is a volume force and $\delta^*=\sqrt{2\nu^*/\omega^*}$ is the conventional thickness of the viscous boundary layer close to the bottom, ν^* being the kinematic viscosity of the fluid.

Using the variables defined by (2), continuity and Navier-Stokes equations become

$$\frac{\partial u_j}{\partial x_j}=0, \tag{3}$$

$$\frac{\partial u_i}{\partial t}+\frac{R_\delta}{2}u_j\frac{\partial u_i}{\partial x_j}=-\frac{R_\delta}{2}\frac{\partial p}{\partial x_i}+\delta_{i1}\sin(t)+\frac{1}{2}\frac{\partial^2 u_i}{\partial x_k \partial x_k}+f_i, \tag{4}$$

where the Reynolds number R_δ is defined by

$$R_\delta=\frac{U_0^*\delta^*}{\nu^*} \tag{5}$$

and δ_{i1} denotes the Kronecker delta. The continuity and momentum equations are solved numerically by means of a finite difference approach in a computational domain of dimensions L_{x1}, L_{x2}, and L_{x3} in the streamwise, spanwise, and vertical directions, respectively. Periodic boundary conditions are enforced in the homogeneous directions (x_1, x_2), because the computational box is chosen large enough to include the largest significant vortex structures of the flow. At the upper boundary, located at $x_3=L_{x_3}$, the free stream condition is enforced as

$$\left(\frac{\partial u_1}{\partial x_3},\frac{\partial u_2}{\partial x_3}\right)=(0,0); \qquad u_3=0 \qquad \text{at} \quad x_3=L_{x_3}, \tag{6}$$

which is equivalent to enforce the vanishing of the shear stresses, since at this elevation the flow is assumed to be irrotational.

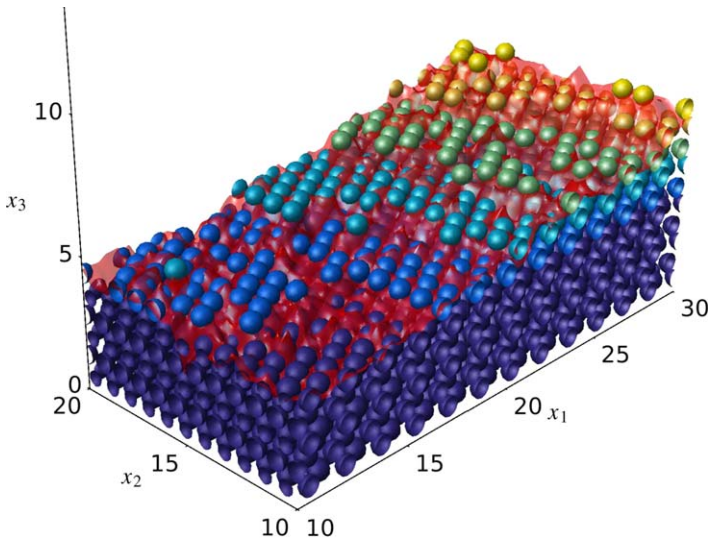

Figure 1. Shown is the numerical reconstruction of the bottom surface captured by laser scanner (red surface) using spheres in the numerical simulation. Warmer (lighter) colors of the spheres indicate larger values of the coordinate x_3 of their centers.

The bottom is assumed to be made up of spherical sediments of size d^* which occupy a small part of the region $x_3^* \geq 0$ and are arranged in such a way that the centers of the sediments on the surface layer are located on a given function $\eta^*(x_1^*, x_2^*)$ (see Figure 1). In particular, 14 layers of spheres were used to mitigate possible over filtration of the fluid through the interstitial spaces between the spheres.

To determine the flow, (3) and (4) are solved throughout the whole computational domain including the space occupied by the solid particles, which are presumed to be immersed in the fluid. Hence, the force terms, f_i, are added to the right-hand side of (4) to enforce the no-slip condition at the fluid-particle interface (immersed boundary approach). At the lower boundary of the fluid domain ($x_3=0$), where a rigid wall is located, the no-slip condition is enforced with

$$(u_1,u_2,u_3)=(0,0,0) \qquad \text{at} \quad x_3=0. \tag{7}$$

The numerical approach solves the problem in primitive variables and uses a second-order fractional-step method to advance the momentum equations in time. The nonsolenoidal intermediate velocity field is evaluated by means of a Crank-Nicolson scheme to

discretize the viscous terms and a three-step, low-storage, self-restarting Runge-Kutta method to discretize explicitly the nonlinear terms. Then, by forcing continuity, (3), a Poisson equation for the pressure field is obtained and solved using a multigrid approach. Once, the pressure field is obtained, the nonsolenoidal velocity field, previously obtained, is corrected to obtain a divergence-free velocity field.

An Adaptive Mesh Refinement (AMR) powered by PARAMESH v4.1 is adopted, enabling an oct-tree-structure local refinement of the numerical grid in the regions of the flow where a fine grid spacing is required according to the Courant-Friedrichs-Lewy condition. The Poisson multigrid solver, which is used to obtain the pressure field, consists of a "global" direct pseudo-spectral solver. "Global" indicates that the problem is defined over the whole domain (i.e., on the finest common grid that can be found in each "local" region of the flow field). Similarly, to obtain the intermediate nonsolenoidal velocity field, a multigrid Helmholtz solver was used, which was developed based on an existing algorithm (Huang & Greengard, 2000) and consists of a global solver, based on the ADI approximate factortization, exploiting a parallel version of Thomas' algorithm, and a local direct solver.

Finally, the immersed boundary (IB) method (Uhlmann, 2005) is used to enforce the no-slip condition on the bed-surface elements. The IB method is implemented using 315 Lagrangian points (i.e., 10 points per particle diameter) to discretize the surface of each sphere and to enforce the vanishing of the velocity. The IB method requires the grid to be equispaced along the three coordinate directions. More details on the numerical approach can be found in Mazzuoli and Vittori (2016). The reliability of both the numerical approach and of the code, which implements it, is verified (Mazzuoli et al., 2017; Mazzuoli & Vittori, 2016) through comparisons with experimental measurements (Keiller & Sleath, 1976) and other numerical results (Fischer et al., 2002; Fornarelli & Vittori, 2009). In particular, both the velocity field and the hydrodynamic forces acting on solid spherical particles were considered in the comparisons and fair agreement with previous results was found.

3. Results and Discussion

The work described herein is aimed at simulating by numerical means the oscillatory flow over a wavy and porous bed for realistic values of the parameters. The topography of the bed surface is chosen by fitting with spherical solid elements (particles) the surface measured by a laser scanner during a laboratory experiment. As already pointed out in the introduction, the use of a direct numerical simulation allows the evaluation of quantities (e.g., vorticity, bottom shear stress, and forces on sediment grains) which are difficult to be measured during a laboratory experiment and provide useful information for the determination of the conditions of incipient sediment motion and the study of sediment dynamics. In particular, several layers of spheres of diameter $d^*=0.7$ mm equal to the mean size of the grains employed in the experiment are located at the vertices of tetrahedrons of side $\ell^*=d^*+2\Delta_d^*$. The small quantity Δ_d^* is introduced for numerical considerations. A region of the experimental bed of sizes 10.75 cm and 0.895 cm in the x_1^* and x_2^* directions, respectively, was reproduced. Since the numerical approach forces periodic boundary conditions in the streamwise and spanwise directions, the measured bottom profile was mirrored in the two horizontal directions and the resulting numerical domain was 21.50 cm long, 1.79 cm wide, and 3.58 cm high.

Figure 1 shows a small portion of the computational domain and the particle arrangement along with the coordinate system while Figure 2 shows a comparison between the experimental bottom profile and the configuration of the granular bed in the numerical simulation along a single vertical plane. The reader should notice that the light gray particles above the solid red line are the particles in the background. The

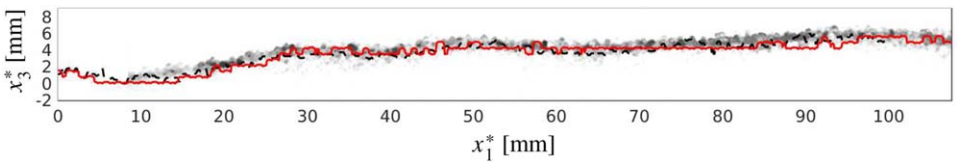

Figure 2. The experimental bottom profile captured by laser scanner (the black dashed line are the sediments at $x_2^*=1.34$ cm while the gray points are the sediments in the background) and the bottom profile approximated by spheres in the numerical simulation (red line).

Table 1
Values of the Parameters for the Present Simulation

R_δ	d	Re_d	ψ	ϱ_s^*/ϱ^*	L_{x_1}	L_{x_2}	L_{x_3}	Δx_{fine}	Δx_{coarse}	No. spheres
246.6	0.78	193.5	6.75	2.65	241.1	20.1	40.2	0.079	0.31	67,907

Note. $Re_d = U_0^* d^*/\nu^*$ is the sphere Reynolds number.

amplitude U_0^* of the velocity oscillations far from the bottom and their period T^* are set equal to 0.28 m s^{-1} and 2.5 s, respectively, as in the experimental apparatus. It follows that the viscous length, δ^*, is equal to 0.89 mm. The grid size close to the bed (the highest resolved region), denoted by Δx_{fine}^*, is equal to 0.07 mm along the three directions, while the coarsest grid, which is employed far from the bottom where the velocity profile is uniform and is denoted by Δx_{coarse}^*, has a size equal to 0.28 mm. The local refinement of the grid did not change during the simulation.

Since sediment particles are fixed, the problem is controlled by two dimensionless parameters, for instance the Reynolds number, $R_\delta = 246.62$, and the dimensionless grain size, $d = 0.78$. The values of the dimensionless parameters in the simulation as well as of the dimensionless size of the computational domain are given in Table 1.

Due to the high computational cost, only 2.11 oscillation periods of the DNS were performed. The simulation was run on 1,024 cores of copper (DoD HPCMP Open Research Systems) and required 4*M* CPU hours. The CFL condition was equal to 0.4. Since the simulation starts from the (laminar) Stokes flow field at $t = 0$, the results of the first cycle are not considered. Even though the gross features of the velocity field measured during the experiment were reproduced by the numerical simulation, a detailed quantitative comparison between the computed and measured flow fields is not possible. Indeed, the high computational costs did not allow the numerical simulation to be carried out for a large number of cycles. Consequently, the phase-averaged flow may not be evaluated. Since the experimental measurements show large differences from cycle to cycle, because of the presence of turbulent eddies and the "chaotic" dynamics of large coherent vortices generated at the bottom, a local and instantaneous comparison also is not possible. However, to justify a quantitative analysis of the numerical results, a qualitative comparison between the numerical results and the experimental measurements were made. Figure 3 shows the experimental values of the streamwise, phase-averaged velocity component plus/minus its standard deviation at two different phases of the cycle ($t = 3.25\pi$ and $t = 3.88\pi$) plotted versus x_3 for $(x_1, x_2) = (170, 15.1)$ along with the instantaneous values provided by the numerical simulation.

Flow visualizations of markers released at different phases of the oscillatory cycle were made to obtain preliminary information on flow structure and mixing processes; however, the analysis of the trajectories of passive tracers cannot be used to reliably identify vortex structures. First, passive tracers were released along two horizontal crossing lines parallel to the x_1 axis and x_2 axis at fixed time intervals, Δt. Tracers were monitored during their motion. The center of the crossing lines is located close to both a trough and a crest of the bottom waviness. The numerical technique employed here mimics the hydrogen bubble technique often used in laboratory experiments. While the procedure does not allow a large portion of the flow to be visualized, it can be used to have a ready visualization of the velocity distribution along the lines of emission and to obtain, so-called smoke lines.

Figures 4a and 4b show top and side views of the positions of the tracers (dye lines) released at $t = 9.74$, when the free stream velocity is near maximum and beginning to decelerate. The tracers were released close to the trough of the bottom waviness and feel a spatial acceleration as the flow moves toward the crest of the bottom waviness. However, the tracers released close to the crest of the bottom waviness feel the effects of a slightly decelerated flow. Since the bottom slope is quite small, both the flow acceleration and deceleration were weak, but the behavior of the two sets of tracers was notably different. In both cases the lines of markers bend and twist because of the vortex structures shed by the roughness elements. The process was quicker for the lines of tracers moving along the lee side of the bottom waviness. At $t = 10.05$, the tracers released close to the crest of the bottom waviness were more fully mixed than those released close to the trough of the bottom waviness. Moreover, the behavior of the tracers depends on the phase of emission during the oscillatory cycle. For example, Figures 5a and 5b exhibit similar behavior to Figures 4a

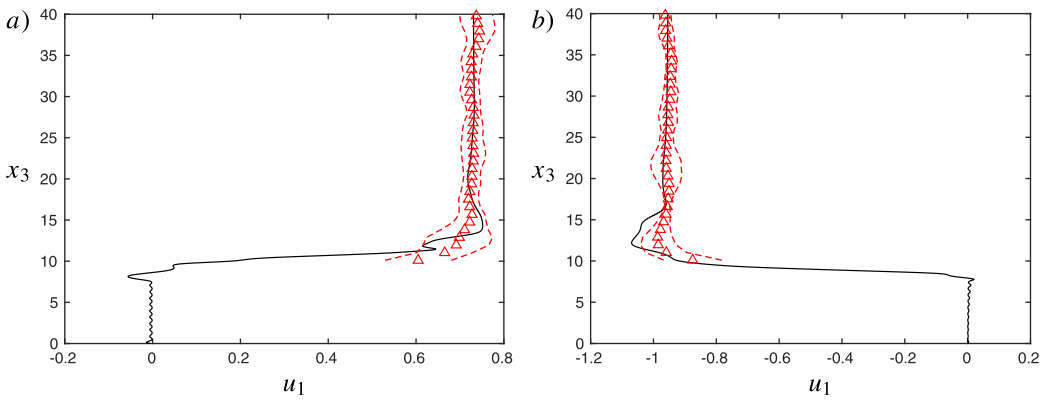

Figure 3. Streamwise component of the velocity plotted versus x_3 along $(x_1, x_2)=(170.0, 15.1)$ at (a) 3.25π and (b) $t=3.88\pi$ for the present simulation (solid black line). Red triangles indicate the phase-averaged values calculated on the basis of the laboratory measurements at the same phases at the corresponding position on the bed. Broken lines indicate the distance of the standard deviation form the averaged value.

and 4b, but the latter are characterized by a phase of emission at $t = 11.62$, suggesting that the mixing process is stronger during the decelerating phase of the cycle than during the accelerating phase. The results show the existence of vortex structures characterized by a strong spanwise vorticity component which tend to roll up the tracers around transverse horizontal axes. In particular, close to flow reversal, the tracers moving along the lee side of the bottom waviness tended to be trapped within a recirculating region formed on the downstream side of the bottom waviness.

Additionally, passive tracers were released in a horizontal plane at $t = 9.07$ along lines parallel to the $x_2$axis equispaced in the streamwise and spanwise directions by δ and lying on the plane $x_3=11.0$. Visualizations of tracer motion at subsequent phases were used to infer the presence of coherent vortices. Figure 6 shows the positions of the tracers at $t = 9.17$. In particular, Figures 6a and 6d show a top view while Figures 6b and 6c show lateral and front views, respectively. In Figures 6a and 6d, it is possible to observe the formation of spanwise bands of tracers traveling in the streamwise direction. The geometry and spacing of the bands suggest the presence of two-dimensional and three-dimensional flow structures characterized by a streamwise wavelength of order $10\delta^*$, which is of the order of magnitude of the size of the most unstable mode predicted by linear stability analysis (Blondeaux & Seminara, 1979) and the resonance mechanism (Blondeaux & Vittori, 1994; Scandura, 2013).

Even though flow visualizations provide interesting information on the oscillatory flow over a rough and wavy bottom, visualization techniques do not provide a complete picture of the dynamics of the vortices characterizing the flow field. Hence, after a preliminary analysis of the flow field using tracer trajectories and streakline patterns, vortex structures were identified by looking at contour surfaces of vorticity (not shown

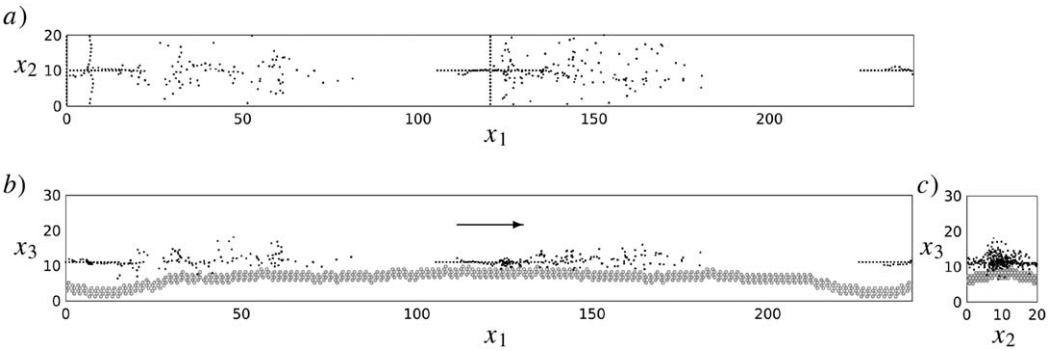

Figure 4. (a) Top, (b) side, and (c) front views of the position of passive tracers released at $t = 9.74$ and then tracked during the deceleration phase at $t=9.80$, 10.05, and 10.37. The positions of the most surficial spheres close to $y=L_y/2$ are visualized by gray small circles. Flow is directed from left to right (see the arrow).

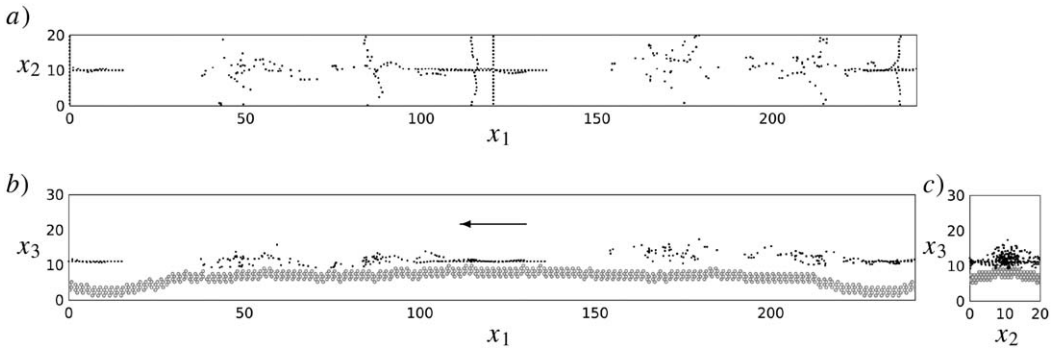

Figure 5. (a) Top, (b) side, and (c) front views of the position of passive tracers released at $t = 11.62$ and then tracked during the acceleration phase at instants t=11.69, 11.94, and 12.25. The positions of the most surficial spheres close to $y=L_y/2$ are visualized by gray small circles. Flow is directed from right to left (see the arrow).

here) and of λ_2, namely the second sorted eigenvalue of the tensor defined by the sum of the squares of the shear rate tensor and of the rigid-like rotation tensor (Jeong & Hussain, 1995).

With the eigenvalues ordered in decreasing value ($\lambda_1 > \lambda_2 > \lambda_3$), Figure 7 shows surfaces characterized by a constant negative value of λ_2 ($\lambda_2 = -0.25$) at different phases of the cycle. At $t = 7.85$ (see Figure 7a), no clear vortex structure can be identified except for the vorticity shed by the sediment grains, and the flow regime may be considered laminar. Close to the end of the accelerating phase, vortex structures appear, which are characterized by a length scale much larger than the roughness size and are originated by an instability of the oscillatory boundary layer (see Figures 7b–7e). The vortex structures pervade larger regions of the bottom surface when the free stream velocity attains its maximum value, and during the decelerating phase, these larger vortices break and form smaller eddies giving rise to small-scale turbulence (Figures 7f and 7g). Later, because of the dissipative effects due to the small eddies, turbulence is damped and the flow tends to relaminarize (Figures 7h and 7i).

Previously, for similar values of the parameters (R_δ=300, 400, $d = 2.32$), simulations of oscillatory flow over spherical particles lying over a plane bed generated a laminar or an only-weakly disturbed laminar flow (Mazzuoli & Vittori, 2016). It is likely that the waviness of the bottom profile simulated here induces spatial accelerations/decelerations of the flow field that trigger the appearance of turbulence for values of the Reynolds number smaller than those characterizing a flat wall (Blondeaux & Vittori, 1994; Scandura, 2013;

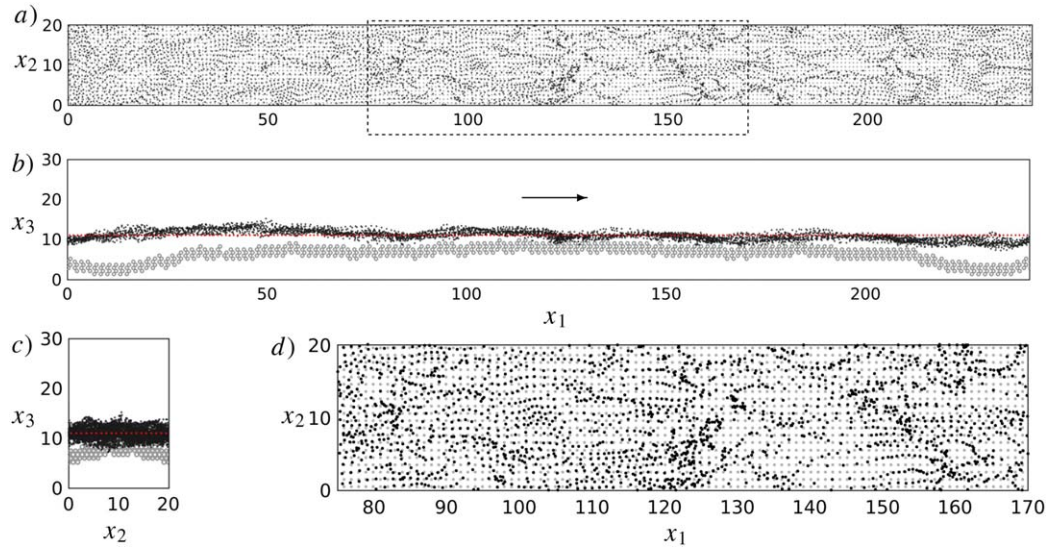

Figure 6. (a) Top, (b) side, and (c) front views of the position of passive tracers released at $t = 9.07$ (gray points) and then plotted at $t = 9.17$ (black points). The positions of the most surficial spheres close to $y=L_y/2$ are visualized by small gray circles. Flow is directed from left to right (see the arrow).

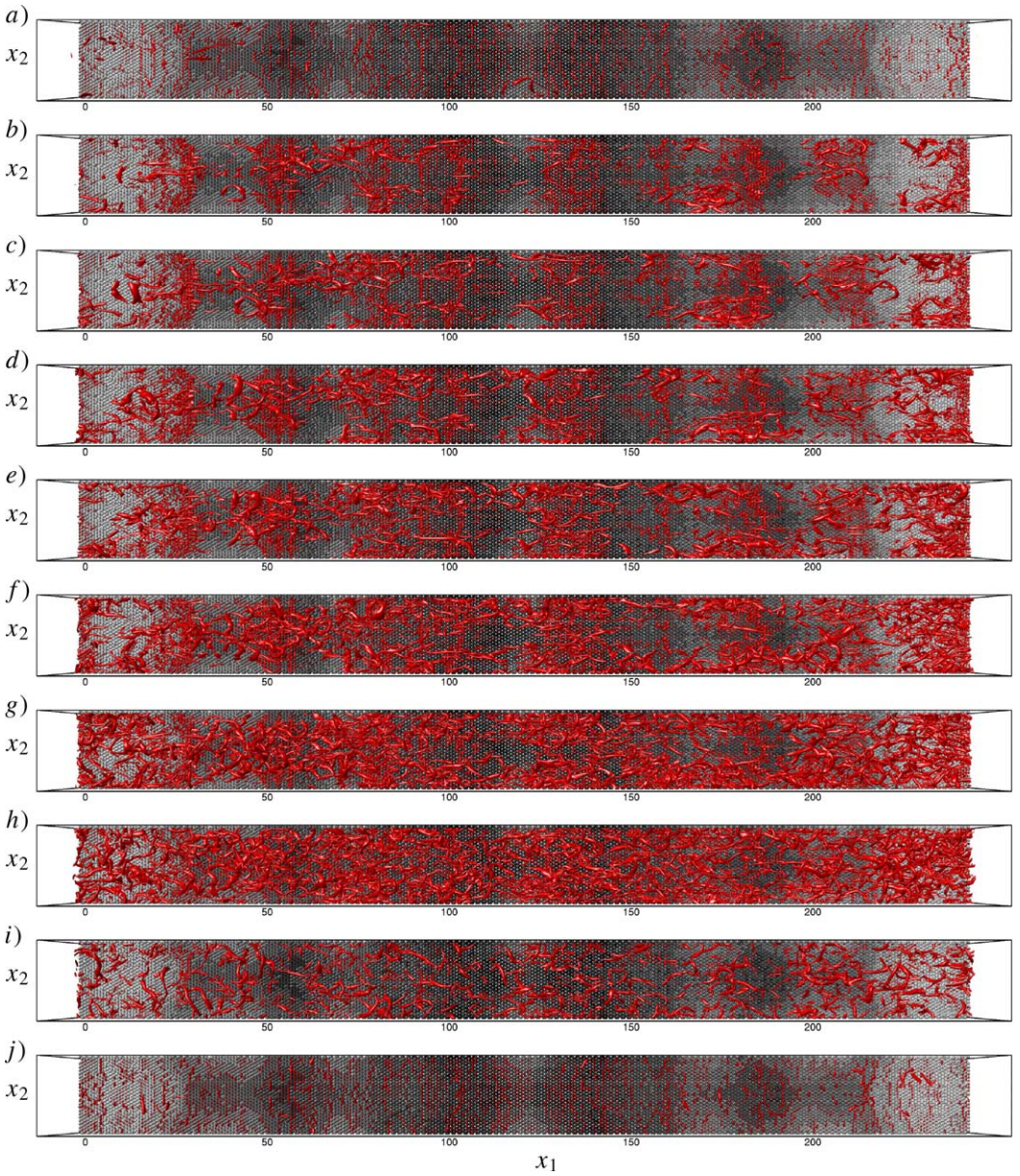

Figure 7. Shown is the top view of the computational domain with vortex structures visualized by isosurfaces for $\lambda_2 = -0.25$ at times (a) $t = 7.85$, (b) $t = 9.11$, (c) $t = 9.19$, (d) $t = 9.27$, (e) $t = 9.35$, (f) $t = 9.42$, (g) $t = 9.58$, (h) $t = 9.94$, (i) $t = 10.41$, and (j) $t = 11.11$.

Scandura et al., 2016; Vittori & Verzicco, 1998). The possible relevance of the bottom undulation in the generation of coherent vortex structures and turbulence appearance is shown by the works of Scandura et al. (2000) and Grigoriadis et al. (2013). In particular, for large values of the free stream velocity, the simulation presented here exhibits complex and multiscale vortices, the dynamics of which appear to be unpredictable. However, the presence of vortex structures which may be defined as "coherent" since they persist in their shape for enough time to be clearly identified. Notably, hairpin vortices of different sizes can be identified in Figures 7d and 7e, which is in agreement with previous observations showing the existence of hairpin vortex structures in turbulent flows close to transition (Head & Bandyopadhyay, 1981; Wu & Moin, 2009a, 2009b). It is believed that these vortex structures are able to generate new vortices because, close to the wall, the tail ends of hairpin vortices converge resulting in fluid eruptions and in the production of new hairpin vortices, thus giving rise to a regenerative process (Marusic, 2001; Perry & Chong, 1982; Townsend, 1980; Zhou et al., 1999). Packets of hairpin vortices in a small region of the computational domain are observed in Figure 8.

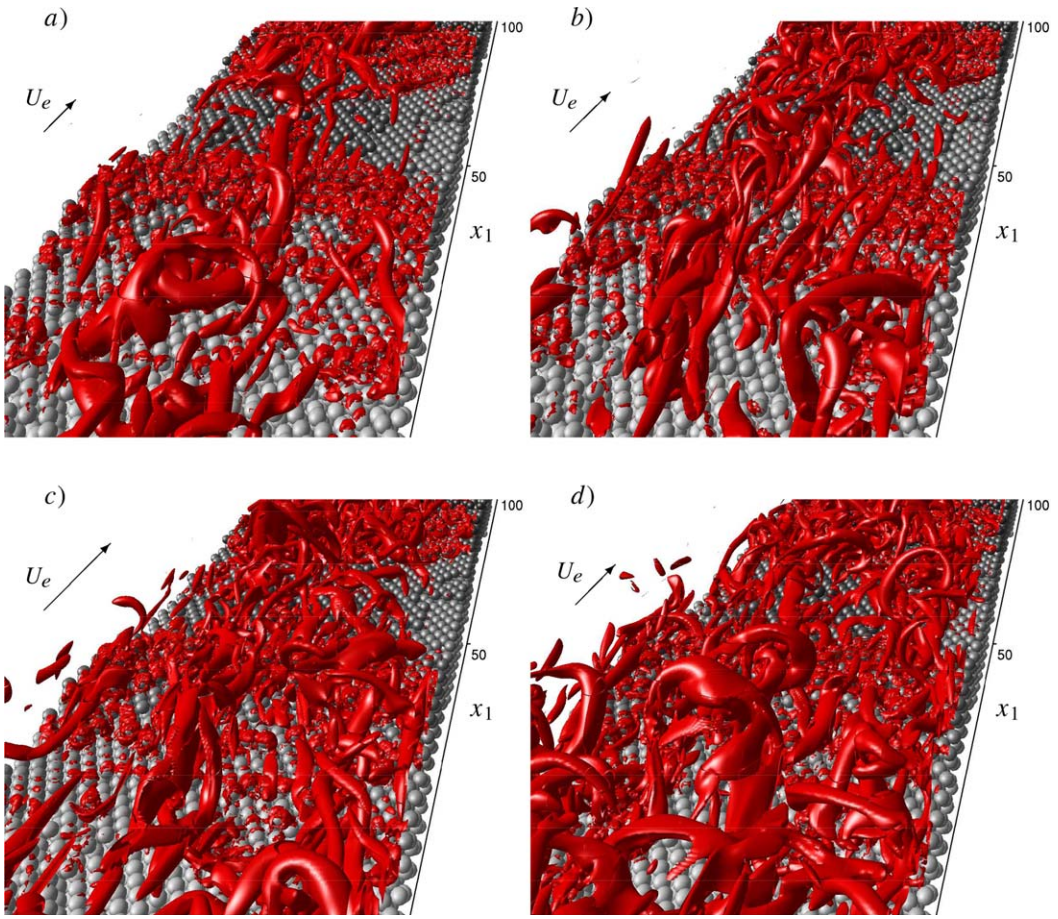

Figure 8. Packets of hairpin vortices in the near-bottom region are visualized by isosurfaces for $\lambda_2 = -0.25$ at (a) $t = 9.24$, (b) $t = 9.40$, (c) $t = 9.47$, and (d) $t = 9.68$.

Turbulence presence for $R_\delta = 246.62$ and $d/\delta = 0.78$ is also in agreement with the transition criteria proposed by various investigators and summarized in Sleath (1988, Figure 13). Indeed, for $d = 1$, Sleath (1988, Figure 13) suggests a critical value of $Re = \frac{U_0^{*2}}{\nu^* \omega^*} \left(= \frac{R_\delta^2}{2} \right)$ for transition to turbulence ranging from about 1,500 ($R_\delta \simeq 55$) to about 20,000 ($R_\delta \simeq 200$).

Because of the high values of the shear they induce, hairpin vortices and other coherent vortex structures which move close to the wall are very efficient in enhancing mixing processes and it is reasonable to assume that they are also a key element in the pickup of sediment particles and in their transport. Figure 9 shows the dynamics of a coherent vortex structure in a particular region of the flow along with the lift force acting on the spherical particles making up the bottom.

The dimensionless hydrodynamic force,

$$\boldsymbol{F}^{(s)} = \frac{6\,\boldsymbol{F}^{*(s)}}{(\varrho_s^* - \varrho^*) g^* \pi d^{*3}}, \tag{8}$$

and torque,

$$\boldsymbol{T}^{(s)} = \frac{24\sqrt{3}\,\boldsymbol{T}^{*(s)}}{(\varrho_s^* - \varrho^*) g^* \pi d^{*4}}, \tag{9}$$

acting on the sth sphere are calculated using their dimensional values $\boldsymbol{F}^{*(s)}$ and $\boldsymbol{T}^{*(s)}$, which are evaluated by integrating over the sphere surface, $\mathcal{S}^{*(s)}$, the stress vector $\boldsymbol{\tau}_n^{*(s)}$ associated with the oriented element of sphere surface $\boldsymbol{n}d\mathcal{S}^*$ and its torque, $\boldsymbol{n}$ and g* denoting the outward-facing unit normal to $d\mathcal{S}^*$ and the

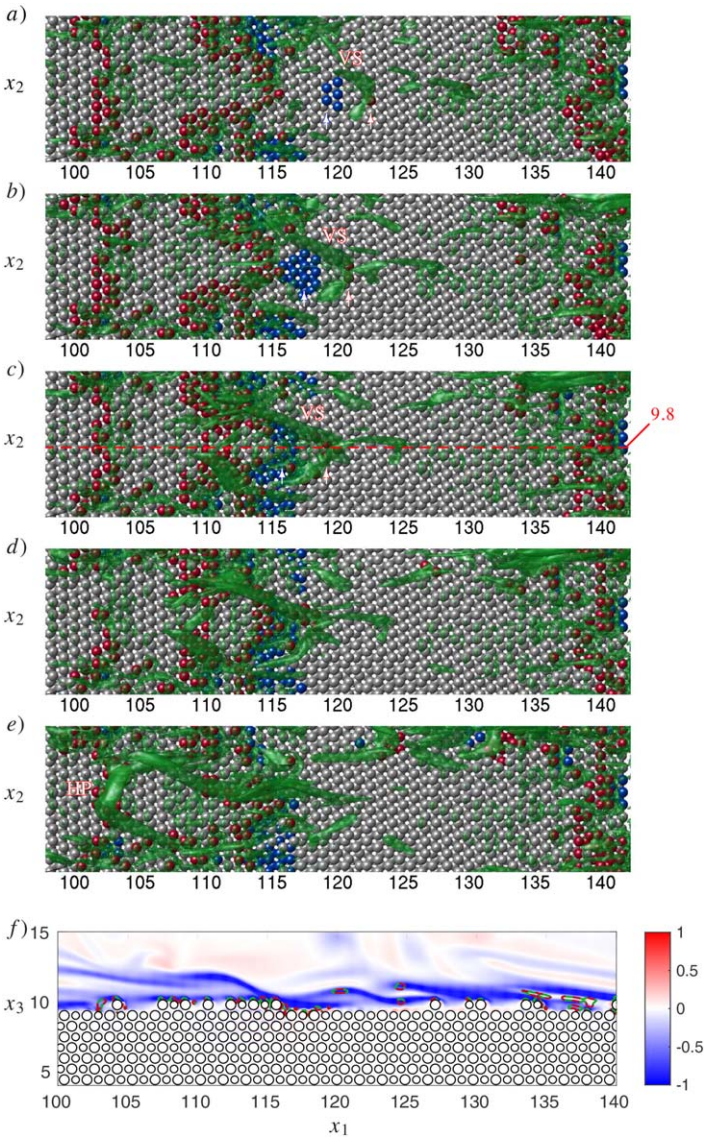

Figure 9. Shown is the top view along a part of the bottom where coherent vortex structures (green contour surfaces for $\lambda_2 = -0.15$) interact with the spheres at time (a) $t = 3.87\pi$, (b) $t = 3.88\pi$, (c) $t = 3.89\pi$, (d) $t = 3.90\pi$, and (e) $t = 3.91\pi$. Spheres are colored by the dimensionless lift force, F_3, when it larger than 0.2 (red) or is smaller than -0.2 (blue). Arrows indicate the footprint of an originating hairpin vortex (HP). (f) shown is a visualization of the spanwise component of the dimensionless vorticity at the plane $x_2 = 9.8$ (indicated by the red broken line in Figure 9c). Green/red contour lines are characterized by $\lambda_2 = -0.25$. The free stream velocity is directed from right to left.

gravitational acceleration, respectively. Since our attention is focused on the ability of the flow to displace sediment particles, the force is scaled with the submerged weight of sediment particles, while torque is scaled with the minimum torque that is necessary to set into rolling motion a sphere lying within a layer of identical spheres arranged in a hexagonal pattern. The results are obtained by fixing the value of the relative density of sediment particles ϱ_s^*/ϱ^* equal to 2.65 and the mobility number of sediment particles $\psi = \frac{U_0^{*2}}{(\varrho_s^*/\varrho^* - 1) g^* d^*}$ equal to 6.75.

In another region of the bottom, a vortex structure named VS, with constant value of λ_2 (iso-λ_2 surface), is visualized in Figure 10 at different phases of the cycle. Simultaneously shown are the sediment particles colored by thresholding the absolute value of normalized lift force, $|F_3|$, above 0.2. The results show that the appearance and dynamics of the coherent vortex structure, VS, have a significant effect on the forces that the flow exerts on sediment grains. The finding is further supported by Figure 11 which shows the time development of the drag and lift forces along with the torque acting on the particle marked by A in Figure 10a. The results indicate that both the drag and lift attain a relative maximum when the coherent vortex structure identified by means of the λ_2-criterion, is above the particle A. However, it should be noted that the vortex structures significantly affect the forces acting on the particles only when they are close to the bottom. Indeed their effects on particle dynamics decrease as they move away from the bottom (see the Movie S1 presently provided as Supporting Information S1).

Since the parameters of the numerical simulation are equal to those of a laboratory experiment during which the sediments did not move, the spherical particles which mimic the sediment were kept fixed. For larger values of the amplitude of the fluid velocity oscillations, the spherical particles would be set into motion and both the velocity field and the forces felt by the particles would be modified by their motion and by the particle-particle collisions (see for example, Mazzuoli et al., 2016).

Significant variations of the drag and lift forces were observed during the oscillatory cycle for the sediment particles on the top-layer that are more exposed to the fluid action. Moreover, because of the three-dimensionality of the bed surface and the "chaotic" dynamics of the coherent vortex structures, the force acting on the spherical particles is expected not to be uniform but to experience fluctuations associated with the position of the particles (geometrical dispersion) and to the turbulent vortices convected by the flow. The time development of the average values of the streamwise and wall-normal force components is shown in Figures 12a and 12b, respectively, along with their standard deviation. The maximum average value of the drag force is shifted by a time interval of $\sim 0.14\pi$ after flow reversal, approximately $\sim 0.11\pi$ before the bottom shear stress predicted by the Stokes solution would be maximum, while the maximum value of the lift force is observed approximately when the free stream velocity attains its maximum value. Moreover, the lift force maintains large values during a significant time interval. Strong fluctuations of the drag force are present when the free stream velocity is maximum. Additionally, the increase in lift fluctuations is approximately in phase with the maximum average lift experienced by the surficial layer of particles, even though it is slightly led by the maximum value of the free stream velocity.

Figures 12c and 12d show the drag and lift force components, respectively, experienced by the highest and lowest spheres of the surficial layer of particles. For the highest sphere, the occurrence of fluctuations

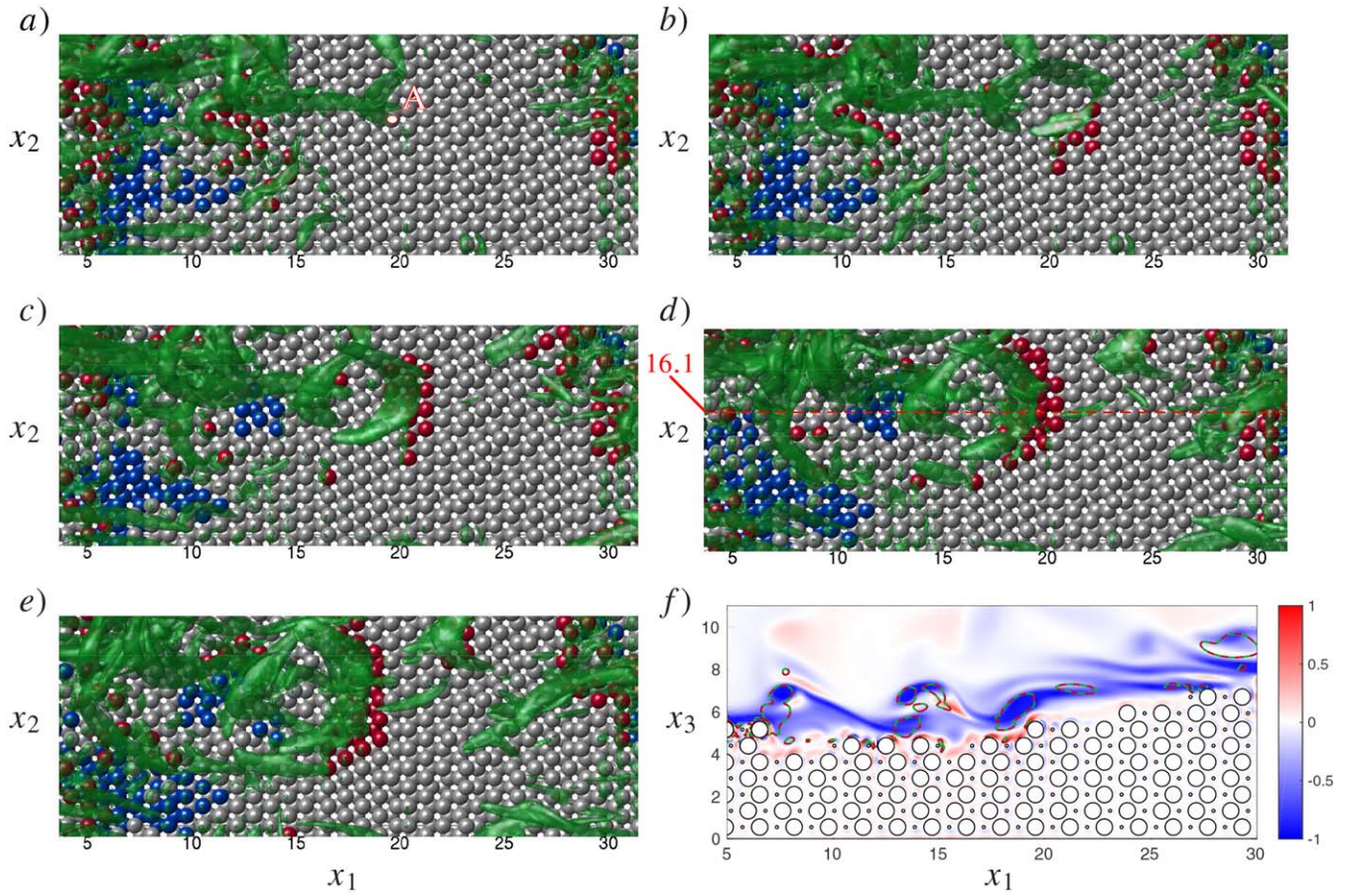

Figure 10. Shown is the top view along a part of the bottom where coherent vortex structures (green contour surfaces for $\lambda_2 = -0.25$) interact with the spheres at time (a) $t = 3.89\pi$, (b) $t = 3.90\pi$, (c) $t = 3.91\pi$, (d) $t = 3.92\pi$, and (e) $t = 3.93\pi$. Spheres are colored by the dimensionless lift force, F_3, when it larger than 0.2 (red) or is smaller than -0.2 (blue). Shown is (f) a visualization of the spanwise component of the dimensionless vorticity at the plane $x_2 = 16.1$ (indicated by the red broken line in Figure 10d). Green/red contour lines are characterized by $\lambda_2 = -0.25$. The free stream velocity is directed from right to left.

reflects the trend of the standard deviation shown in Figures 12a and 12b, but for the lowest sphere the fluctuations are quite small and sporadic. As previously noted, the bottom waviness triggers the appearance of turbulence and makes the flow more similar to that of the hydraulically rough regime previously observed (see Mazzuoli & Vittori, 2016, Figures 16 and 26). The results for the drag and lift forces on spherical particles presently simulated ($d^* = 0.625\delta^*$) are qualitatively different for $R_\delta = 400$ and $d = 2.32$, but

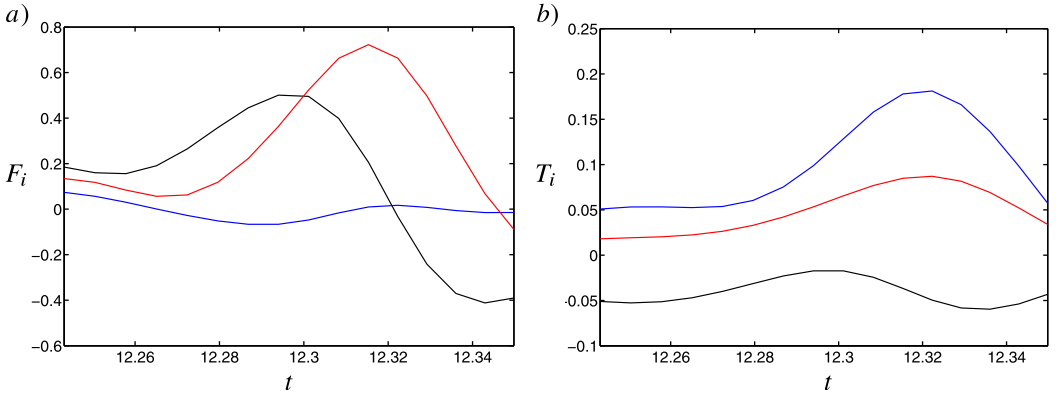

Figure 11. Shown are the components, i equal to 1 (black), 2 (blue), and 3 (red) of the (a) force and (b) torque acting on the sphere marked by A in Figure 10a.

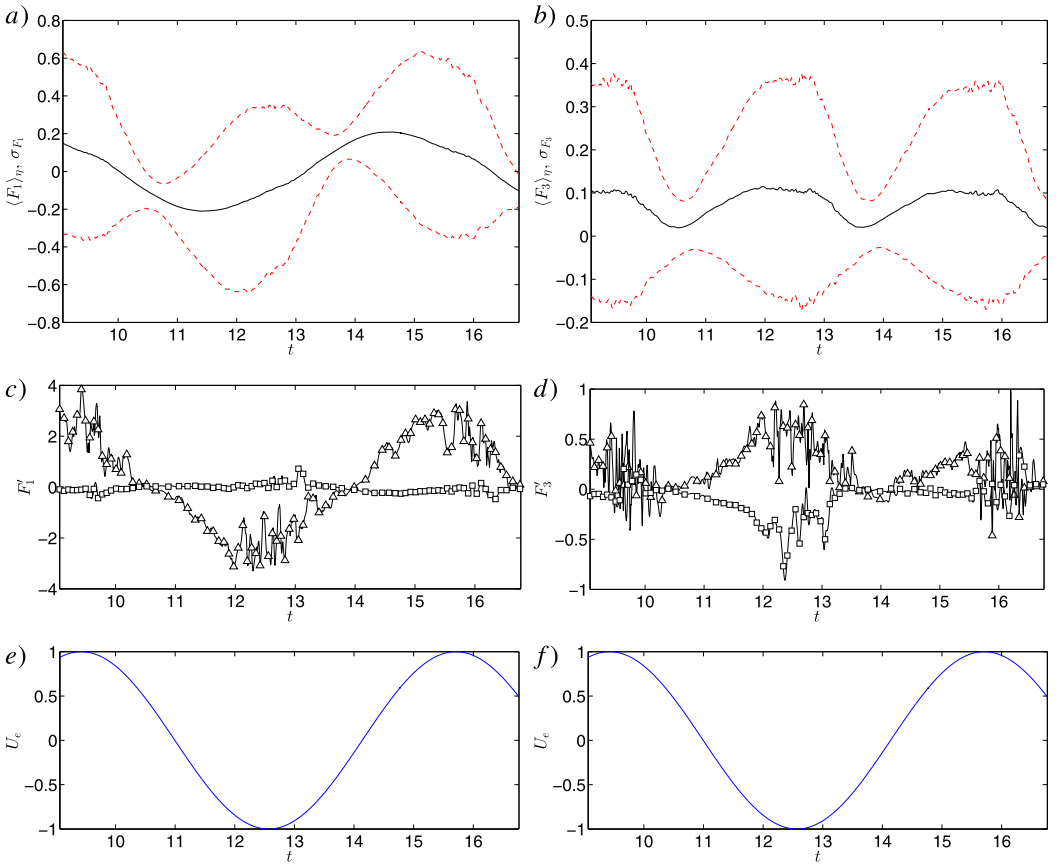

Figure 12. Spatial average (black) and standard deviation (dashed red) of (a) drag and (b) lift forces acting on the top-layer of spheres are plotted as functions of time. Also plotted are the values of the fluctuations of (c) drag and (d) lift forces associated with the highest (–△–) and lowest (–□–) spheres of the top-layer. (e, f) The time development of the principal mean velocity far from the bottom.

similar for $R_\delta = 400$ and $d = 6.95$, where large fluctuations of the drag and lift forces were observed (Mazzuoli & Vittori, 2016). In particular, simulations were characterized by strong fluctuations for $R_\delta = 400$, which is a value of the Reynolds similar to the present one, and referred such flow a regime as *hydraulically rough* (Mazzuoli & Vittori, 2016). The main difference in our simulation is that not all the spheres contribute evenly to the statistics of force acting on the spherical particles.

The numerical results show also that it would be quite difficult to identify the conditions of incipient sediment motion by increasing the amplitude of the fluid displacement oscillations. Indeed, by increasing the value of U_0/ω, a value would be encountered so that the lift force would become larger than the submerged weight (dimensionless values of F_3 larger than one) and a few particles would be dislodged from their equilibrium position at a particular phase of the cycle. However these conditions would be met just for a few particles which would stop after a small displacement and no general motion of the sediments would be observed. Further increases of U_0/ω would lead to an increase of the number of moving particles but a well-defined "critical value" would be difficult to be identified, the process being continuous.

It has been asserted that the "random waviness" of the bottom configuration plays a prominent role in triggering the appearance of turbulence and the forces that would cause the motion of the spherical particles, which mimic the sediment grains in the simulation. The bottom waviness causes a few particles to be more exposed than other particles, but the local separation of the viscous bottom boundary layer, which is observed even when the bottom is assumed to be flat from a macroscopic point of view, anticipates turbulence appearance. Moreover, it was verified that below the top-layer of the spheres, the fluid velocity drops

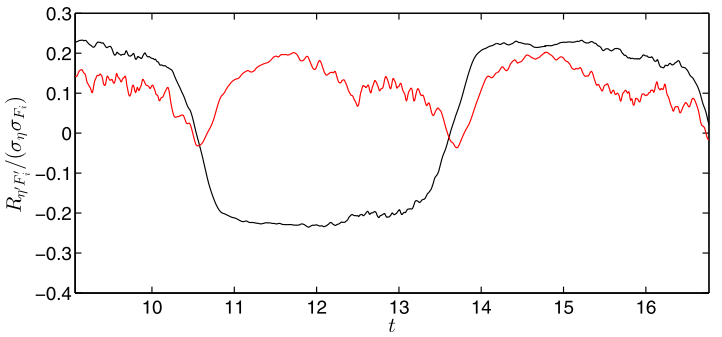

Figure 13. Plotted as a function of time is the cross correlation between the distance of the top-layer of spheres from the average bed elevation and the respective fluctuations of drag ($i = 1$, black) and lift ($i = 3$, red) forces, scaled by the product of the respective standard deviations.

to small values and the drag force almost coincides with the contribution due to the pressure-gradient oscillations. Therefore, flow resistance is dominated by the interaction of the flow with the top-layer of spheres.

In order to quantify the influence of the bed geometry on the deviation of the hydrodynamic force from the mean value, the normalized cross correlations between the distance η' of the top-layer spheres from the average bed elevation and the fluctuations of drag and lift force components are plotted in Figure 13 as functions of time. The cross-correlation functions, denoted in Figure 13 by $R_{\eta' F_1'}$ and $R_{\eta' F_3'}$, show that a correlation equal to ∼25% exists between positive values of η' and drag fluctuations while the correlation between η' and lift fluctuations is ∼20%. The correlation includes both the effect of spatial dispersion associated with the geometrical features of the bed surface and the effect of turbulent fluctuations induced by the interaction of the spheres with the vortex structures. Figures 14a and 14b show the normalized probability density functions of the drag and lift fluctuations at time, $t = 15.92$, when the streamwise velocity far from the bottom is almost maximum. The fluctuations of drag and lift of small magnitude and slightly negative occurred much more frequently than strong fluctuations which were predominantly characterized by a positive value. Similar features were previously observed in the in the context of steady, turbulent open-channel flow (Chan-Braun et al., 2011); however, the effect of the bed geometry considered here makes the pdfs deviate significantly from a Gaussian distribution.

The results shown here suggest that fluctuations of the lift force acting on the spheres and the position of the spheres with respect to the flow can determine the conditions for individual sediment particles to be picked up. Moreover, it appears that the sediments can be set into motion under the action of turbulent vortex structures that interact with the bed in relatively small portions of the bed surface. Since sea waves have wavelengths much longer than the typical wavelength of the morphological patterns present on the seafloor including those tested in the experimental apparatus described above, it is reasonable to reduce the effect of the small morphological patterns to that of a supplementary roughness. This presumption allows us to collect the statistics of quantities that are relevant for the problem of sediment transport (e.g., the shear stress) on bottom parallel planes regardless of the position of bed forms. The amount of sediments set into motion by the flow is usually correlated with the shear stress of the flow at a certain elevation near the bottom. Consequently, the incipient condition for sediment transport is often estimated, in the absence of direct measurements, on the basis of empirical or semiempirical predictors, which consider

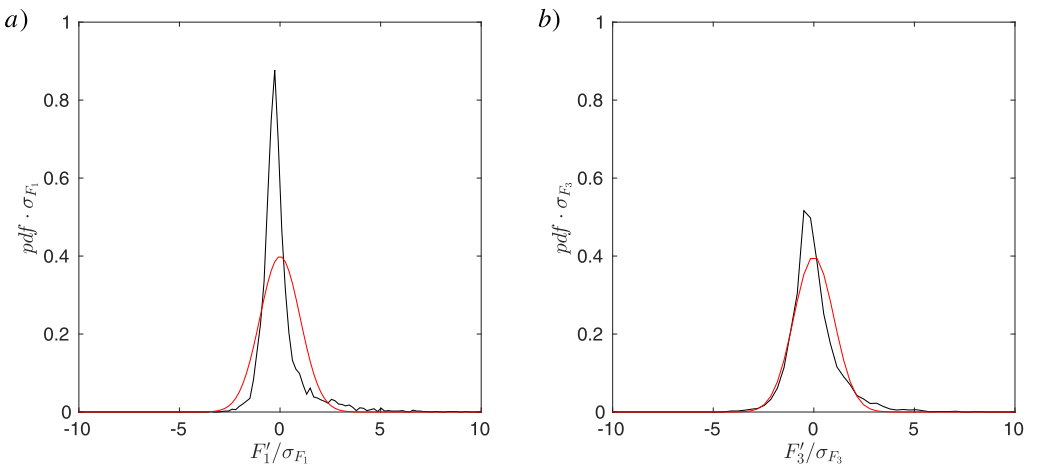

Figure 14. Shown is the normalized probability density functions (black) of fluctuations of (a) drag and (b) lift forces acting on the top-layer of spheres at $t = 15.92$. Red lines indicate the Gaussian distributions characterized by average equal to 0 and the value of the standard deviation of the respective distributions of force fluctuations.

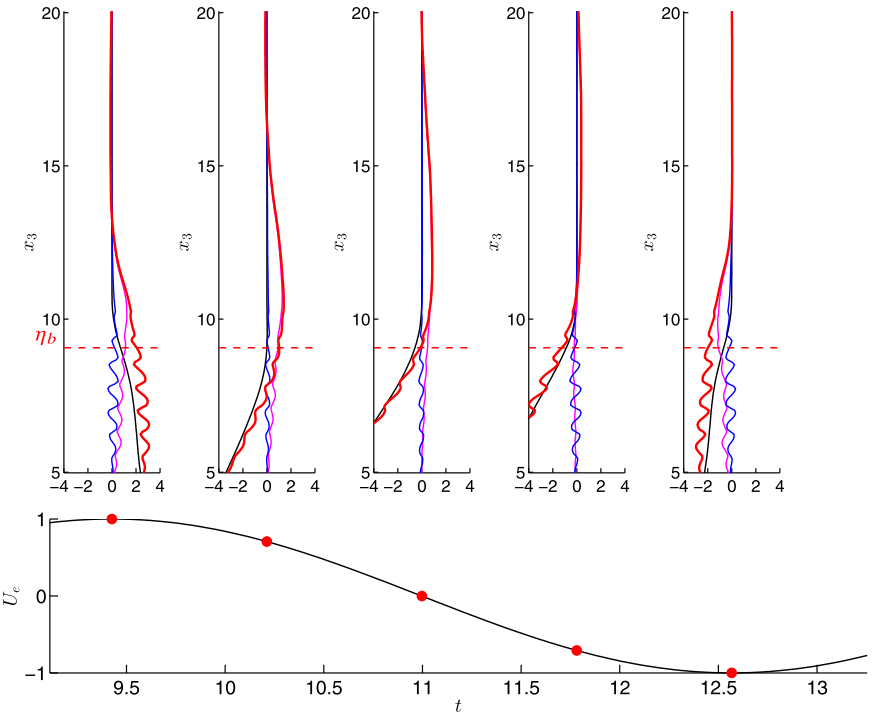

Figure 15. Shown is the momentum balance, integrated from the top of the computational domain toward the wall, plotted as a function of the wall-normal coordinate, computed at different phases of the wave cycle (lower). The total shear stress, τ_{tot} (red thick) is equal to the sum of the viscous (blue) and Reynolds shear stress (magenta) plus the contribution of the volume force associated with the spheres (black).

the shear stress experienced by the bed. The bed shear stress is estimated at an average bed elevation, η_b (e.g., the elevation at which the spanwise-averaged solid volume fraction reaches the value 0.1). In the present case, the total bed shear stress can be computed from the streamwise component of the Reynolds equation. By splitting the variables u_i, p, and f_i into their plane-averaged values $\langle u_i \rangle$, $\langle p \rangle$, and $\langle f_i \rangle$, and their fluctuating u_i', p', and f_i' values. Continuity and momentum equations lead to

$$\frac{\partial \langle u_1 \rangle}{\partial t} - \sin(t) = -\frac{R_\delta}{2}\frac{\partial \langle u_1' u_3' \rangle}{\partial x_3} + \frac{1}{2}\frac{\partial^2 \langle u_1 \rangle}{\partial x_3^2} + \langle f_1 \rangle, \tag{10}$$

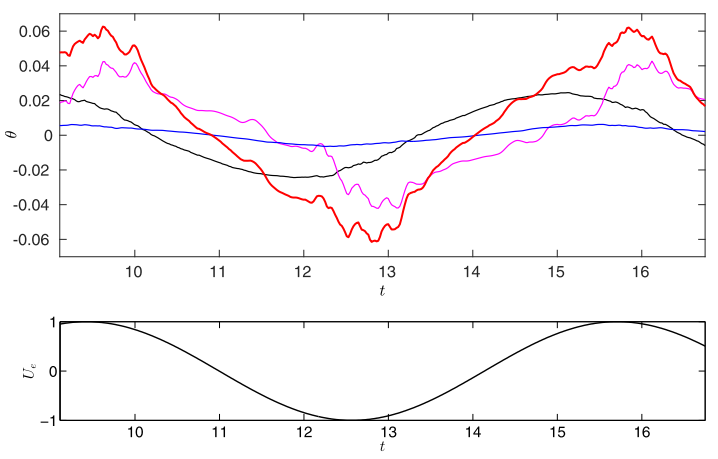

Figure 16. The contributions shown in Figure 15 at the distance $x_3 = \eta_b = 9.06$ from the wall are plotted as a function of time.

where the last term is computed by transferring the Lagrangian hydrodynamic forces that spheres apply on the flow field onto the Eulerian grid. Then, by integrating (10) from L_{x_3} downward to x_3, the dimensionless total shear stress $\tau_{tot} = \tau_{tot}^* / \left(\frac{1}{2}\varrho^* U_0^* \omega^* \delta^*\right)$ at x_3 is readily obtained

$$\tau_{tot} = \left.\frac{\partial \langle u_1 \rangle}{\partial x_3}\right|_{x_3} - R_\delta \langle u_1' u_3' \rangle|_{x_3} + 2\int_{x_3}^{L_{x_3}} \langle f_1 \rangle \, dx_3 \tag{11}$$

and it turns out to be the sum of a viscous contribution (first term on the right-hand side), a turbulent contribution (second term on the right-hand side), and a contribution due to the action of the spherical sediments on the fluid motion (last term on the right-hand side).

The values of τ_{tot} and those of the different contributions to it are plotted along x_3 at different phases of the cycle in Figure 15. The results show that the contribution due to the viscous stress is negligible everywhere but within the porous bed where the packed spheres

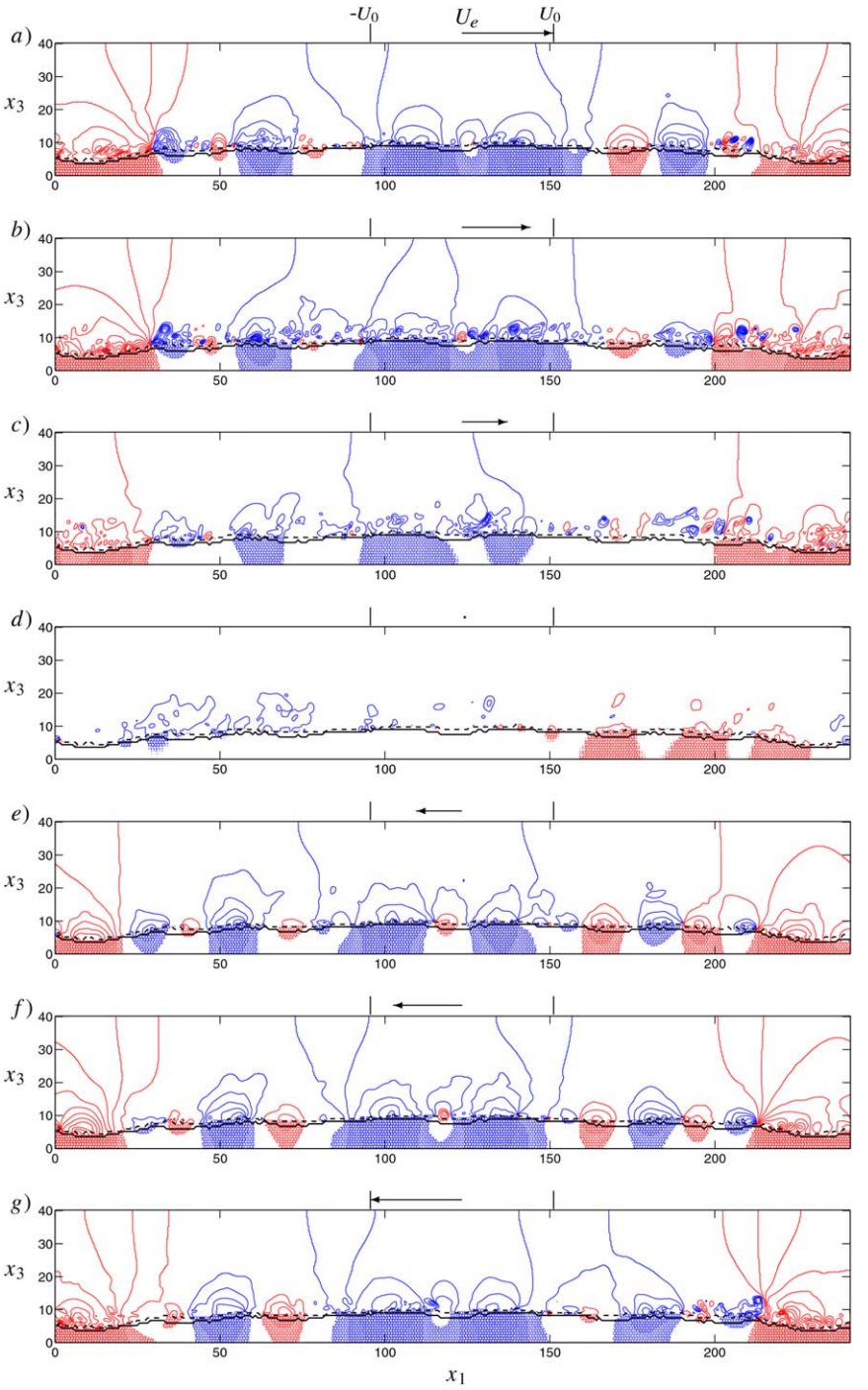

Figure 17. Distribution of pressure p at the plane $x_2=L_{x_2}/2$ and at time (a) $t=3\pi$, (b) $t=25/8\pi$, (c) $t=13/4\pi$, (d) $t=7/2\pi$, (e) $t=15/4\pi$, (f) $t=31/8\pi$, and (g) $t=4\pi$. Positive and negative pressure regions are indicated by red (solid) and blue (broken) contour lines, respectively, equispaced by 0.02. The maximum and minimum elevation of the bed is visualized by the solid and broken black lines, respectively. The instantaneous direction and intensity of the free-stream velocity U_e is qualitatively displayed over each figure.

slow down the fluid velocity. Far from the bottom, the contribution due to the presence of turbulence dominated the flow up to the region where the irrotational flow is found. Finally, the contribution due to the sediment grows linearly moving within the bottom since the fluid velocity is small and only the grain-grain interaction balances the pressure-gradient effect.

The time development of the Shields parameter, θ, namely the total bed shear stress, τ^*_{tot} at $x_3^*=\eta_b^*$ normalized by $(\varrho_s^*-\varrho^*)g^*d^*$ is shown in Figure 16. Figure 16 shows that if the waviness of the bottom is filtered out by the average operation and the contribution to the total shear stress due to the spherical particles is not considered, it is likely that no sediment transport takes place. However, by including the contribution $\left(2\int_{x_3}^{L_{x_3}}\langle f_1\rangle\ dx_3\right)$ due to the sediment particles, it is likely that a few sediment grains become eligible to be set into motion when the free stream velocity and the Reynolds shear stress attain their maximum values. Indeed, even though the critical value of the Shields parameter depends on the Reynolds number of the sediment, the value 0.05 is often considered in sediment transport formulae and the exclusion/inclusion of the contribution due to the spherical particles makes the Shields parameter smaller/larger than 0.05. It is also worth pointing out that the maximum of the viscous stress lagged behind the maximum of the free stream and the stress associated with the spherical particles attains its maximum value even earlier, as shown in Figure 12a. In other words, a prediction of the sediment transport rate which does not take into account the local turbulent events related to the bed profile could lead to significant underestimation of the sediment flux.

Other quantities of interest provided by the numerical simulation are the pressure and flow fields within the porous bed. The relative pressure, p_a-p_0, may be expressed as the sum of two contributions,

$$p_a-p_0=p_w+p\,, \tag{12}$$

where p_0 denotes an arbitrary constant value, p_w is the contribution which grows/decays linearly in the streamwise direction and drives the free stream oscillations, and p is the pressure field that appears in (4). The pressure p depends on (x_1,x_2,x_3) because of the flow spatial accelerations/decelerations induced by the waviness of the bottom profile and by the large-scale vortex structures which characterize the turbulent flow (see Figure 7). Pressure variations are also associated with the interstitial flow between the spherical particles. However, the seepage flow through the porous bed is quite small and these pressure fluctuations are almost negligible. Indeed, if v^*_{sp} denotes the order of magnitude of the seepage flow velocity, the pressure variations are expected to have an order of magnitude equal to $\rho^* v^{*2}_{sp}$.

Figure 17 shows the pressure field, p, at different phases of the cycle both above and within the porous bed. When the free stream velocity is large (either positive or negative) the pressure in the trough of the bottom profile is positive. It assumes negative values over the crest of the forcing to generate the pressure gradient which is necessary to accelerate the flow from the trough to the crest. Then, small spatial fluctuations can be recognized, which are induced either by a locally small waviness of the bottom or by the presence of large-scale coherent vortex structures. These small pressure oscillations can be more easily identified when the external velocity is relatively small. Moreover, the results show that the pressure oscillations are almost constant in the vertical direction when moving within the porous bed, since the seepage flow is very weak.

4. Conclusions

A direct numerical simulation of the oscillatory flow over a wavy, rough, and porous bed made up of small spherical particles was used to obtain the following results about the near bed flow structures and their effect on particle stability. (i) The bottom waviness is found to play an important role in the transition process to turbulence even if the amplitude and slope of the bottom undulation are quite small (the amplitude was about five grain diameters); in particular, the appearance of turbulence was triggered for values of the Reynolds number smaller than the critical values for a flat bed. (ii) Close to the bottom, the flow was dominated by the vortex structures shed by the sediment grains and those generated by the transition process to the turbulent regime. (iii) At moderate values of the Reynolds number, the oscillatory boundary layer tended to relaminarize when the large turbulent vortex structures break and generate small eddies that dissipate due to viscous effects. The phenomenon takes place just after the free stream velocity attains its maximum value and lasts almost until flow reversal. (iv) Transition to turbulence generates coherent vortex structures (hairpin vortices), which increase mixing phenomena (e.g., momentum transfer) and have a significant effect on the force and torque felt by sediment grains. (v) The force and torque experienced by the surficial sediment particles were found to be strongly correlated to the elevation of the particles relative to the mean bed elevation. (vi) The fluctuations of the force acting on sediment grains were found to be large relative to their average value, suggesting that the conditions of incipient motion based on average quantities would not be appropriate. (vii)

The force fluctuations are related to both the elevation of individual grains and the passage of the turbulent vortex structures close to the bed. (viii) Finally, the flow within the porous bed is found to be quite small and the forces generated by the applied pressure gradient on the sediment grains are balanced by the grain-grain interaction. The numerical simulations provide detailed information on the flow-bed profile-sediment interaction, which cannot be easily obtained by means of laboratory experiments, and can be used to improve the modeling of sediment transport and the predictors of the sediment transport rates.

Acknowledgments
This study has been funded by the Office of Naval Research (U.S.; under the research projects N6290914PR00165 and 1000006450). Julian Simeonov and Joe Calantoni were supported under base funding to the U.S. Naval Research Laboratory by the Office of Naval Research. This work was supported in part by a grant of computer time from the DoD High Performance Computing Modernization Program at the ERDC DSRC. The data used are listed in the references, tables, supporting information, and repository at http://www.dicca.unige.it/~markom/MazzuoliEtAl_JGR/.

References

Blondeaux, P. (2001). Mechanics of coastal forms, *Annual Review of Fluid Mechanics*, *33*(1), 339–370.
Blondeaux, P., & Seminara, G. (1979). Transizione incipiente al fondo di un onda di gravità. *Rendiconti dell'Accademia Nazionale dei Lincei*, *67*, 107–417.
Blondeaux, P., & Vittori, G. (1991). Vorticity dynamics in an oscillatory flow over a rippled bed. *Journal of Fluid Mechanics*, *226*, 257–289.
Blondeaux, P., & Vittori, G. (1994). Wall imperfections as a triggering mechanism for stokes-layer transition. *Journal of Fluid Mechanics*, *264*, 107–135. https://doi.org/10.1017/S0022112094000601
Chan-Braun, C., García-Villalba, M., & Uhlmann, M. (2011). Force and torque acting on particles in a transitionally rough open-channel flow. *Journal of Fluid Mechanics*, *684*, 441–474. https://doi.org/10.1017/jfm.2011.311
Fischer, P. F., Leaf, G. K., & Restrepo, J. M. (2002). Forces on particles in oscillatory boundary layers. *Journal of Fluid Mechanics*, *468*, 327–347.
Fornarelli, F., & Vittori, G. (2009). Oscillatory boundary layer close to a rough wall. *European Journal of Mechanics: B/Fluids*, *28*(2), 283–295. https://doi.org/10.1016/j.euromechflu.2008.06.002
Ghodke, C. D., & Apte, S. V. (2016). Dns study of particle-bed–turbulence interactions in an oscillatory wall-bounded flow. *Journal of Fluid Mechanics*, *792*, 232–251.
Grigoriadis, D., Balaras, E., & Dimas, A. (2013). Coherent structures in oscillating turbulent boundary layers over a fixed rippled bed. *Flow, Turbulence and Combustion*, *91*(3), 565–585.
Head, M., & Bandyopadhyay, P. (1981). New aspects of turbulent boundary-layer structure. *Journal of Fluid Mechanics*, *107*, 297–338.
Huang, J., & Greengard, L. (2000). A fast direct solver for elliptic partial differential equations on adaptively refined meshes. *SIAM Journal of Scientific Computation*, *21*(4), 1551–1566.
Jeong, J., & Hussain, F. (1995). On the identification of a vortex. *Journal of Fluid Mechanics*, *285*, 69–94. https://doi.org/10.1017/S0022112095000462
Keiller, D. C., & Sleath, J. F. A. (1976). Velocity measurements close to a rough plate oscillating in its own plane. *Journal of Fluid Mechanics*, *73*(4), 673–691. https://doi.org/10.1017/S0022112076001560
Krstic, R., & Fernando, H. (2001). The nature of rough-wall oscillatory boundary layers. *Journal of Hydraulic Research*, *39*(6), 655–666.
Le Hir, P., Monbet, Y., & Orvain, F. (2007). Sediment erodability in sediment transport modelling: Can we account for biota effects? *Continental Shelf Research*, *27*(8), 1116–1142.
Marusic, I. (2001). On the role of large-scale structures in wall turbulence. *Physics of Fluids*, *13*(3), 735–743.
Mazzuoli, M., Blondeaux, P., Simeonov, J., & Calantoni, J. (2017). Direct numerical simulation of the oscillatory flow around a sphere resting on a rough bottom. *Journal of Fluid Mechanics*, *822*, 235–266.
Mazzuoli, M., Kidanemariam, A. G., Blondeaux, P., Vittori, G., & Uhlmann, M. (2016). On the formation of sediment chains in an oscillatory boundary layer. *Journal of Fluid Mechanics*, *789*, 461–480.
Mazzuoli, M., & Vittori, G. (2016). Transition to turbulence in an oscillatory flow over a rough wall. *Journal of Fluid Mechanics*, *792*, 67–97.
Mei, C. C., & Liu, P. (1993). Surface waves and coastal dynamics. *Annual Review of Fluid Mechanics*, *25*(1), 215–240.
Nielsen, P. (1992). *Coastal bottom boundary layers and sediment transport*. Singapore, Singapore: World Scientific.
Perry, A., & Chong, M. (1982). On the mechanism of wall turbulence. *Journal of Fluid Mechanics*, *119*, 173–217.
Scandura, P. (2013). Two-dimensional vortex structures in the bottom boundary layer of progressive and solitary waves. *Journal of Fluid Mechanics*, *728*, 340–361.
Scandura, P., Faraci, C., & Foti, E. (2016). A numerical investigation of acceleration-skewed oscillatory flows. *Journal of Fluid Mechanics*, *808*, 576–613.
Scandura, P., Vittori, G., & Blondeaux, P. (2000). Three-dimensional oscillatory flow over steep ripples. *Journal of Fluid Mechanics*, *412*, 355–378.
Sleath, J. F. (1984). *Sea bed mechanics*. New York, NY: John Wiley.
Sleath, J. F. (1988). Transition in oscillatory flow over rough beds. *Journal of Waterway, Port, Coastal, and Ocean Engineering*, *114*(1), 18–33.
Soldati, A., & Marchioli, C. (2009). Physics and modelling of turbulent particle deposition and entrainment: Review of a systematic study. *International Journal of Multiphase Flow*, *35*(9), 827–839. https://doi.org/10.1016/j.ijmultiphaseflow.2009.02.016
Soldati, A., & Marchioli, C. (2012). Sediment transport in steady turbulent boundary layers: Potentials, limitations, and perspectives for lagrangian tracking in dns and les. *Advances in Water Resources*, *48*, 18–30.
Townsend, A. A. (1980). *The structure of turbulent shear flow*. Cambridge, UK: Cambridge University Press.
Uhlmann, M. (2005). An immersed boundary method with direct forcing for the simulation of particulate flows. *Journal of Computational Physics*, *209*(2), 448–476. https://doi.org/10.1016/j.jcp.2005.03.017
Vittori, G., & Blondeaux, P. (1993). Quasiperiodicity and phase locking route to chaos in the 2-D oscillatory flow around a circular cylinder. *Physics of Fluids A: Fluid Dynamics*, *5*(8), 1866–1868.
Vittori, G., & Verzicco, R. (1998). Direct simulation of transition in an oscillatory boundary layer. *Journal of Fluid Mechanics*, *371*, 207–232.
Wu, X., & Moin, P. (2009a). Direct numerical simulation of turbulence in a nominally zero-pressure-gradient flat-plate boundary layer. *Journal of Fluid Mechanics*, *630*, 5–41.
Wu, X., & Moin, P. (2009b). Forest of hairpins in a low-reynolds-number zero-pressure-gradient flat-plate boundary layer. *Physics of Fluids*, *21*(9), 091106.
Zhou, J., Adrian, R. J., Balachandar, S., & Kendall, T. (1999). Mechanisms for generating coherent packets of hairpin vortices in channel flow. *Journal of Fluid Mechanics*, *387*, 353–396.